Soft Matter

PAPER

View Article Online
View Journal

Cite this: DOI: 10.1039/c4sm00952e

Buckling of an elastic rod embedded on an elastomeric matrix: planar *vs.* non-planar configurations†

Tianxiang Su,‡§[a] Jia Liu,‡[a] Denis Terwagne,‡¶[b] Pedro M. Reis*[bc] and Katia Bertoldi*[ad]

Received 2nd May 2014
Accepted 20th June 2014

DOI: 10.1039/c4sm00952e

www.rsc.org/softmatter

We investigate the buckling of a slender rod embedded in a soft elastomeric matrix through a combination of experiments, numerics and theory. Depending on the control parameters, both planar wavy (2D) or non-planar coiled (3D) configurations are observed in the post-buckling regime. Our analytical and numerical results indicate that the rod buckles into 2D configurations when the compression forces associated to the two lowest critical modes are well separated. In contrast, 3D coiled configurations occur when the two buckling modes are triggered at onset, nearly simultaneously. We show that the separation between these two lowest critical forces can be controlled by tuning the ratio between the stiffness of the matrix and the bending stiffness of the rod, thereby allowing for specific buckling configurations to be target by design.

1 Introduction

A slender fiber can buckle under axial compression even when embedded, and therefore supported, inside an elastomeric matrix.[1–3] As a result, planar periodic configurations (2D) have been observed in microtubules,[4,5] fiber-reinforced composites,[6–8] and pipelines on seabeds.[9,10] Non-planar coiled configurations (3D) have also been observed from the buckling of other constrained rodlike structures, including: plant roots growing in soil,[11] packaged DNA in viruses,[12] and coil tubing in oil-field operations.[13,14] Interestingly, it has recently been shown that a silicon nano-wire attached to a soft substrate[15] can exhibit either planar or non-planar configurations, depending on the stiffness of the substrate, which can be tuned. Finding both 2D and 3D configurations in the same system raises the fundamental question regarding the conditions under which an embedded fiber can buckle in-plane or out-of-plane. From a practical perspective, modern nano-devices that include rodlike components can be used for sensors, resonators and electromagnetic wave absorbers.[16–18] Rationalizing the post-buckling regime in this class of embedded filamentary structures could therefore open opportunities for functionality by generating complex 3D shapes, reversibly and on-demand.

Here, we investigate the mechanical response, under compression, of a single elastic fiber (rod) embedded in an elastomeric matrix. We seek to rationalize the conditions under which either planar or non-planar buckling configurations are attained, depending on the combined stiffnesses of the matrix and the rod. Throughout, we assume that no delamination occurs between the rod and the matrix. We start by performing precision model experiments where a Nitinol rod is embedded within a polydimethylsiloxane (PDMS) cylinder, and the ensemble is compressed uniaxially. Our experiments reveal that for matrices that are sufficiently stiff (with respect to the bending stiffness of the rod) the rod buckles directly onto a non-planar coiled configuration. By contrast, with softer matrices, both 2D and 3D buckling configurations can be observed. Moreover, we find that the morphology of the buckled patterns and their associated characteristic length scales can be tuned by changing the geometric and material parameters of the system. These results are rationalized by a model based on the classic Winkler foundation.[19] Our analysis suggests that non-planar configurations are triggered when the critical buckling loads associated to the first two eigenmodes become comparable. This hypothesis is tested numerically by performing both dynamic simulations and finite element analyses. The simulations confirms that the separation between the two lowest critical loads determines whether a rod buckles in-plane or out-of-plane. Moreover, the numerical results highlight the

[a]School of Engineering and Applied Sciences, Harvard University, Cambridge, MA, 02138, USA. E-mail: bertoldi@seas.harvard.edu
[b]Department of Civil and Environmental Engineering, Massachusetts Institute of Technology, Cambridge, MA, 02139, USA. E-mail: preis@mit.edu
[c]Department of Mechanical Engineering, Massachusetts Institute of Technology, Cambridge, MA, 02139, USA
[d]Kavli Institute for Bionano Science and Technology, Harvard University, Cambridge, MA, 02138, USA

† Electronic supplementary information (ESI) available. See DOI: 10.1039/c4sm00952e

‡ These authors contributed equally to this work.

§ Current address: Schlumberger-Doll Research Center, Cambridge, MA, 02139, USA.

¶ Current address: Faculté des Sciences, Université Libre de Bruxelles (ULB), Bruxelles 1050, Belgium.

important effect of the boundary conditions and the presence of shear deformation in the matrix in setting the observed buckling patterns.

2 Experiments

2.1 Experimental setup

In Fig. 1 we present a photograph of the experimental apparatus that we used to uniaxially compress our samples. Each sample consisted of a slender Nitinol rod that was concentrically embedded inside an elastomeric cylinder (the matrix) made out of polydimethylsiloxane (PDMS). We fabricated, characterized and tested a total of 15 samples for which we changed the stiffness of the matrix, as well as the radius and length of the rod (see Table S1† for detailed geometric and material properties). Upon compression, the Nitinol rod buckled within the matrix and the process was imaged by two perpendicular digital cameras. Representative configurations from the two orthogonal views are shown in the insets of Fig. 1.

Each experimental sample contained a SE508 Nitinol rod that is 10 cm long. At both ends of the sample, the rod was made to pass through a tight clearance hole centered on an acrylic disk, onto which it was glued, which ensured clamped boundary conditions. We used five Nitinol rods with radii and Young's moduli in the ranges $25.4 < r_r$ [μm] < 127, and $59 < E_r$ [GPa] < 78, respectively (see ESI for exact values†). Nitinol is known for its unique hyperelastic and shape memory properties.[20,21] Given that all experiments were performed at constant room temperature, $T = 20$ °C, we did not make use of its shape memory characteristics. Hyperelasticity, on the other hand, was important since it confers reversibility to the experimental tests, even for the geometrically nonlinear configurations observed in the post-buckling regime.

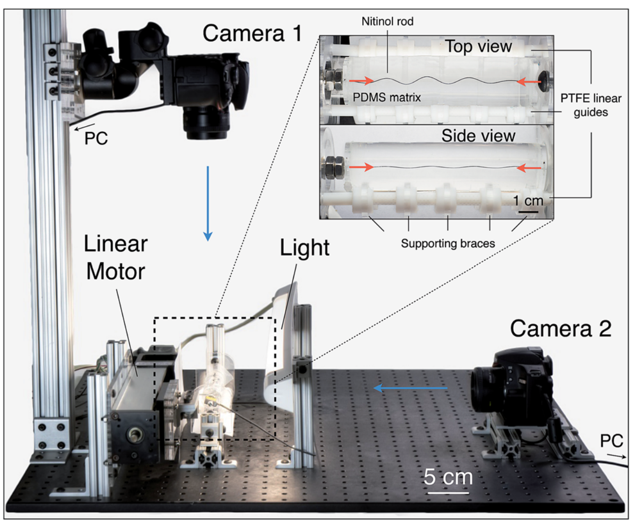

Fig. 1 Experimental apparatus. A Nitinol rod is embedded within a cylindrical PDMS matrix (inside dashed frame). The sample is uniaxially compressed under displacement control. Two synchronized cameras placed on the top and side of the setup capture snapshots of the buckling of the rod (insets). The paired images are then sent to a computer for reconstruction of the configuration of the rod and further analysis.

The elastomeric matrix (10 cm long and 2.6 cm in diameter) was cast in a cylindrical mold using PDMS (Sylgard 184 from Dow Corning Inc.), with the Nitinol rod held in between the two acrylic disks, along the central axis. Using PDMS had the advantage that its Young's modulus can be tuned during fabrication by varying the relative mixture of base and curing agents, from 0.4 kPa to 3 MPa (ref. 22) (see Fig. S1†). In our experiments, however, we focused on the range $17 < E_m$ [kPa] < 84, which enabled us to fully explore the post-buckling regime of the rod under compression, while preventing delamination between the Nitinol and the PDMS matrix. Moreover, this range ensured that the samples could be supported horizontally, without significant deflection under their own weight.

Once fabricated, the samples were mechanically tested on a custom-made uniaxial compression device (Fig. 1). Each sample was laid horizontally on top of a series of five independent acrylic braces that were set perpendicular to the axis of compression (see inset of Fig. 1). These braces supported the sample and could slide along the axis of compression using two PTFE (polytetrafluoroethylene) linear guides. A computer controlled linear stage uniaxially compressed the whole sample (matrix, rod and acrylic disks). Each test was performed quasi-statically under conditions of controlled displacement. Note that our setup differs from a previous study,[23] where only the rod, without the matrix, was compressed.

During each experimental test, two perpendicular digital cameras were synchronized to acquire images of the Nitinol rods (one from the side and the other from above, as shown in Fig. 1) at every 0.1 mm step of compression. The pairs of frames were then combined and image-processed to produce 3D reconstructions of the coordinates of the rod. Two representative examples of the reconstructed configurations rods in the planar and non-planar regimes are presented in Fig. 2A and B, respectively. From the 3D reconstructions we could readily measure the wavelength of the buckled configurations, as well as the pitch of the non-planar shapes. Moreover, to further facilitate the analysis (described in more detail below), we also performed a Principal Component Analysis (PCA)[24,25] that rigidly rotates the configuration of the rod, without distortion, such that its major lateral buckling direction is always aligned with the global horizontal y-axis.

2.2 Experimental results

Both 2D and 3D buckling configurations of the Nitinol rod were observed during the uniaxial compression of our samples. In Fig. 2A and B, we present two representative configurations obtained for samples #1 and #2 (see Table S1†), respectively, at $\varepsilon = 3\%$ compressive strain. Sample #1 buckled into a periodic planar configuration, whereas sample #2 buckled into a non-planar configuration, with deformation in the two orthogonal lateral directions.

The buckling shapes of each sample are further characterized by computing the ellipse of minimum area that encloses the cross-sectional view of the buckled rod at $\varepsilon = 3\%$ (dashed

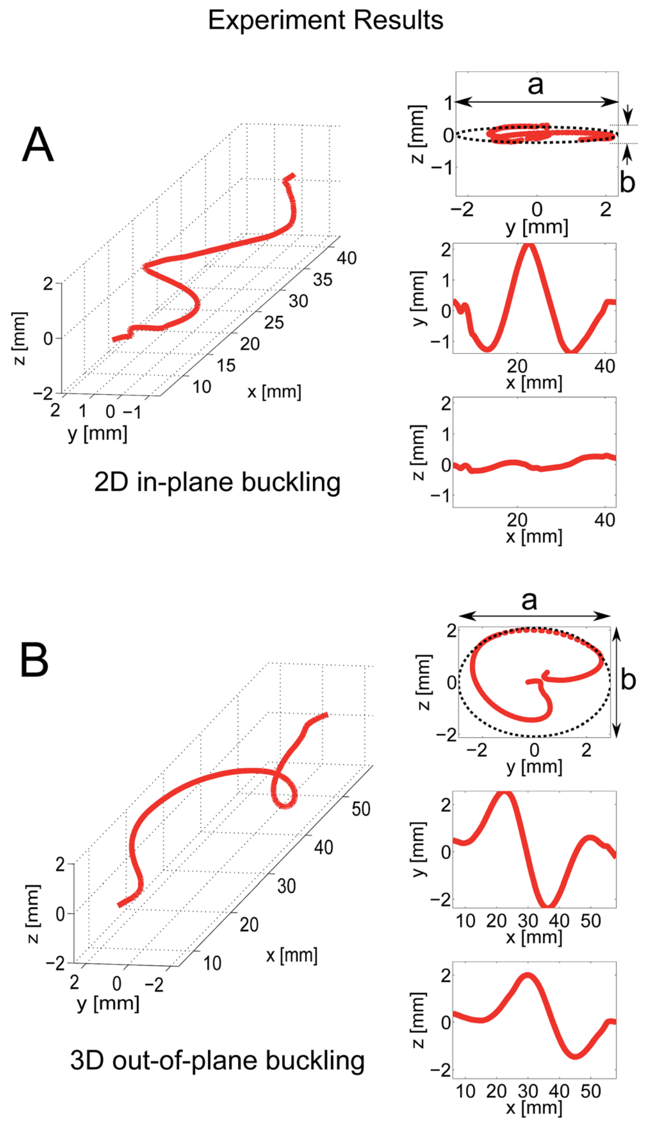

Fig. 2 Experimental results. Buckled configurations of (A) sample #1 and (B) sample #2 acquired at $\varepsilon = 3\%$ compressive strain. Both 3D and projected views (onto the z–y, y–x and z–x) are shown, clearly indicating that sample #1 buckles into a 2D planar configurations, while sample #2 buckles into a 3D coiled configuration. The dashed ellipse shown in the y–z view corresponds to the ellipse with minimum area that encloses the cross-sectional projection of the rod.

line in the cross-section views in Fig. 2A and B, see ESI for details†). The aspect ratio, b/a, between the minor and major axes of this ellipse, quantifies the extent to which the buckled shape is 2D or 3D. A flat ellipse ($b/a \ll 1$) indicates a planar configuration, while a more circular one ($b/a \sim 1$) indicates that it is fully 3D.

In Fig. 3A, we report the aspect ratio, b/a, for all 15 samples, as a function of their dimensionless matrix stiffness (rationalized in detail in Section 3, below),

$$\eta = \frac{E_m L_r^{\,4}}{E_r I_r}, \tag{1}$$

where E_m is the Young's modulus of the matrix and E_r, I_r and L_r are the Young's modulus, second moment of area and length of the rod, respectively. The experimental results reveal that: (i) for stiff matrices ($\eta > 5 \times 10^6$) all samples are characterized by large values of b/a, indicating a coiled, non-planar buckling shape; (ii) for $\eta < 5 \times 10^6$, both small and large values for b/a are observed, indicating that both planar and non-planar configurations can occur. Whereas the finding (ii) is consistent with previous qualitative observations for a nanowire attached to a soft substrate,[15] the finding (i) is, to the best of our knowledge, reported here for the first time.

We proceed by quantifying the wavelength, λ, of the buckled configurations, which we plot in Fig. 3B for all samples as a function of the dimensionless matrix stiffness, η, at $\varepsilon = 3\%$ compressive strain. Interestingly, the results for both planar and non-planar buckling configurations collapse onto the same curve that is consistent with a power-law $\lambda \sim \eta^{-1/4}$, which we will show in Section 3 can be rationalized and derived analytically.

Summarizing the experimental results thus far, we have found that the dimensionless stiffness $\eta = E_m L_r^{\,4}/(E_r I_r)$ determines whether the rod buckles into a planar or a non-planar configuration and it also sets the characteristic length scales of the buckling pattern. We now seek to rationalize these results and proceed by investigating the effect that the stiffness of the matrix has on the mechanical response of the system, first analytically (Section 3) and later numerically (Section 4). The important role played by the boundary conditions will then be discussed in more detail in Section 5.

3 Theoretical analysis

Towards rationalizing the conditions that lead to 2D and 3D buckling configurations, we adopt the Winkler foundation model[19] of a thin and stiff beam supported by a softer elastic substrate. Moreover, the treatment of our elastomeric matrix is simplified as an array of springs with stiffness K acting solely in radial direction.

Assuming small strains and moderate rotations, the governing equation for the embedded elastic rod is given by,[19]

$$E_r I_r \frac{\partial^4 Y}{\partial S^4} + F\frac{\partial^2 Y}{\partial S^2} + KY = 0, \tag{2}$$

where F is the applied compressive force and Y and S denote the lateral displacement and the arc length of the rod, respectively. Introducing the normalized displacement, $y = Y/L_r$, and arc length, $s = S/L_r$, allows for eqn (2) to be rewritten in dimensionless form,

$$\frac{\partial^4 y}{\partial s^4} + \pi^2 f\frac{\partial^2 y}{\partial s^2} + \pi^4 k y = 0, \tag{3}$$

where $f = FL_r^{\,2}/(\pi^2 E_r I_r)$ and $k = KL_r^{\,4}/(\pi^4 E_r I_r)$ are the dimensionless compressive force and spring constant, respectively. When both ends of the rod are free to rotate, the solution of eqn (3) has the form $y(s) = A\sin(n\pi s)$, with n denoting the mode number.

Substituting $y(s)$ into eqn (3), yields the compressive force required to trigger the n-th mode,[19]

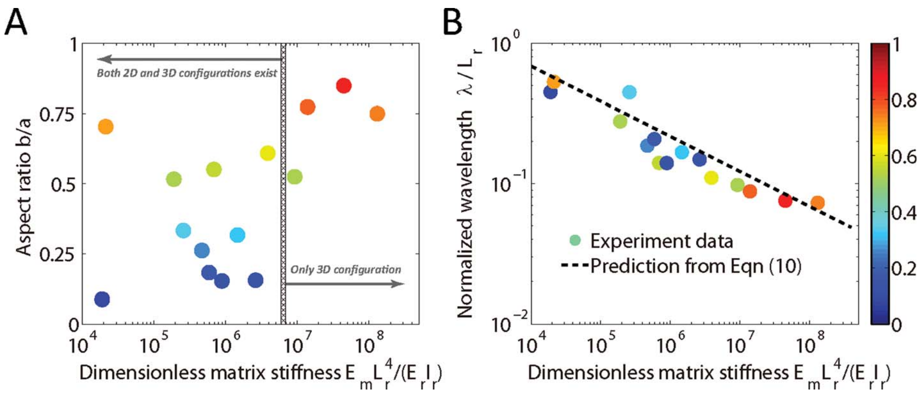

Fig. 3 Characteristic length scales of the buckled samples. (A) Ratio between the minor and major axes of the minimum area ellipse that encloses the cross-sectional view at $\varepsilon = 3\%$ as a function of the normalized matrix stiffness $\eta = E_m L_r^4/(E_r I_r)$. Small b/a values indicate a planar buckling configuration, while large values of b/a correspond to 3D coiled configurations. (B) Normalized buckling wavelength λ/L_r as a function of the normalized matrix stiffness η. Excellent agreement is found between the experimental results (data points) and the analytical prediction (dashed black line – eqn (10)) obtained using the Winkler foundation model. The color of the markers indicates the corresponding b/a value for each sample, as given by the adjacent color bar.

$$f_n = n^2 + \frac{k}{n^2}, \tag{4}$$

which can be alternatively obtained using an energy approach[26,27](see ESI for details†). Given that the mode associated to the lowest f_n emerges and grows during loading, the critical buckling force for the system is given by,

$$f_{cr} = \min_{n=1,2,\ldots} \left(n^2 + \frac{k}{n^2} \right). \tag{5}$$

Even though this result is well known in the literature, we turn our focus to the fact for specific values of k, there can be two possible modes associated to f_{cr}. In Fig. 4A, we further highlight this point by plotting the dependence of the dimensionless difference, $\Delta f/f_{cr} = (f_{n'} - f_{cr})/f_{cr}$, between the lowest ($f_{cr}$) and second lowest ($f_{n'}$) compressive forces, as a function of k. We find that for the specific values of the normalized spring constant,

$$k = m^2(m+1)^2,\ m = 1, 2, 3, \ldots \tag{6}$$

$\Delta f/f_{cr}$ vanishes, such that the system is degenerated and two different modes, m and $m + 1$ say, are both associated with the same critical compressive force, $f_{cr} = f_m = f_{m+1}$. As a result, two buckling modes are triggered simultaneously at the onset of instability and we expect them to interact with one another[28] to produce non-planar (3D) configurations.

The above interpretation is supported by our experimental results since in all cases of 3D coiled configurations, two neighboring modes were observed to grow in perpendicular directions. For example, the configuration shown in Fig. 2B exhibits the orthogonal modes $m = 2$ and $m = 3$, simultaneously. In contrast, when k is far from the specific values given

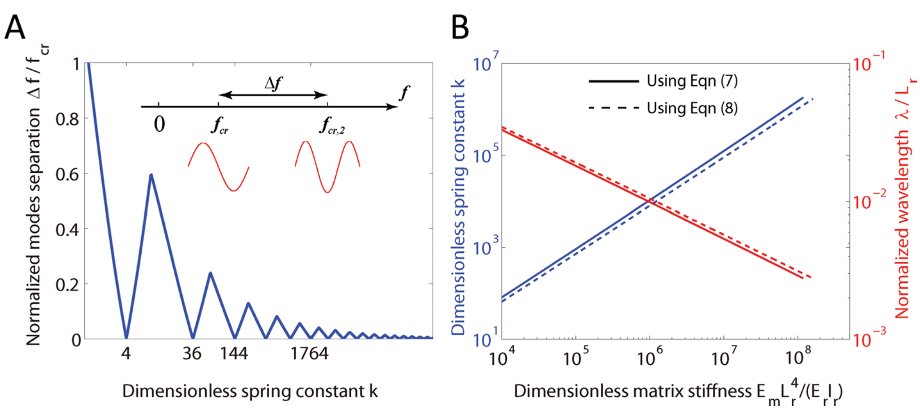

Fig. 4 Theoretical results. (A) Normalized separation of the critical forces associated with the two lowest modes, $\Delta f/f_{cr}$, as a function of the dimensionless matrix spring constant k. The Winkler foundation model as been used and the rod has free-to-rotate ends. For some specific values of k (provided by eqn (6)) $\Delta f = 0$, so that two modes are triggered simultaneously at the buckling onset. (B) Dimensionless spring constant k (blue lines) and wavelength λ/L_r (red lines) as function of $\eta = E_m L_r^4/(E_r I_r)$ for a rod with radius $r_r = 101.5\ \mu m$. Solid and dashed lines correspond to the prediction obtained using eqn (7) and (8), respectively.

by eqn (6), the critical forces for adjacent modes are sufficiently separated such that only a single mode is expected to be triggered and grow, resulting in a 2D planar buckling configuration. It is also interesting to note that the maxima of $\Delta f/f_{\rm cr}$ plotted in Fig. 4A decrease for increasing values of k. Consequently, rods embedded in stiff matrices are expected to always buckle into non-planar configurations, which is also consistent with the experimental results reported in Fig. 3A (for $\eta > 5 \times 10^6$).

The relation between our analysis and the experimental results can now be made more quantitative. We make use of existing results for the spring stiffness,[6,7]

$$K = \frac{16\pi G_{\rm m}(1-\nu_{\rm m})}{2(3-4\nu_{\rm m})K_0(n\pi r_{\rm r}/L_{\rm r}) + n\pi r_{\rm r} K_1(n\pi r_{\rm r}/L_{\rm r})/L_{\rm r}}, \quad (7)$$

arising when a rod of radius $r_{\rm r}$ and length $L_{\rm r}$ buckles into mode n inside a matrix with shear modulus $G_{\rm m} = E_{\rm m}/[2(1+\nu_{\rm m})]$, where $K_0(\cdot)$ and $K_1(\cdot)$ are the modified Bessel functions and $E_{\rm m}$ and $\nu_{\rm m}$ are the Young's modulus and Poisson's ratio of the matrix, respectively. In the limit of a slender rod, *i.e.* $r_{\rm r}/L_{\rm r} \to 0$, eqn (7) can be further simplified (see ESI for details†) to

$$K = \frac{8\pi G_{\rm m}(1-\nu_{\rm m})}{\ln(2L_{\rm r}/nr_{\rm r})}, \quad (8)$$

which has been recently used to study buckling of confined microtubules (assuming $\nu_{\rm m} = 0.5$).[5]

Eqn (7) and (8) indicate that K depends on both $G_{\rm m}$ and n, suggesting that attaining a general description for all buckling modes may be challenging. However, a unique relation between the wavelength of the mode, $\lambda = 2L_{\rm r}/n$, and the spring and matrix stiffness can indeed be determined upon calculation of the mode number that minimize f_n (*i.e.* determining the values of n for which $\partial f_n/\partial n = 0$). In particular, minimization of f_n using eqn (8) yields,

$$\frac{(\lambda/L_{\rm r})^4(2\ln(\lambda/r_{\rm r})-1)}{[\ln(\lambda/r_{\rm r})]^2} = \frac{24\pi^3}{\eta}, \quad (9)$$

where $\eta = E_{\rm m}L_{\rm r}{}^4/E_{\rm r}I_{\rm r}$ is the dimensionless stiffness of the matrix introduced earlier in eqn (1). Eqn (9) can be solved iteratively to obtain λ for a given set of matrix and rod properties.

This analysis reveals that λ depends on both the dimensionless stiffness of the matrix, η, and the radius of the rod, $r_{\rm r}$, but the dependence on the latter is found to be weak. As a result, we can further simplify eqn (9) to

$$\frac{\lambda}{L_{\rm r}} = \alpha\eta^{-1/4}, \quad (10)$$

where the prefactor α is found to depend weakly on $\lambda/r_{\rm r}$. For example, in our experiments where $134.4 < \lambda/r_{\rm r} < 432.8$, the prefactor can be calculated to lie within $6.71 < \alpha < 7.04$. Given this limited range for α, and without loss of generality, for the reminder of this analysis we choose $\lambda/r_{\rm r} = 240$, for which $\alpha = 6.88$. Note that an almost identical prediction for the wavelength (*i.e.* $\lambda/L_{\rm r} = 6.62\eta^{-1/4}$) has been obtained using an energy approach and a nonlinear von Karman formulation to model the rod[26] (see ESI for details†).

In Fig. 4B we plot the evolution of the dimensionless spring constant, $k = KL^4/(\pi E_{\rm r}I_{\rm r})$, (left axis) and the buckling wavelength, λ, (right axis) as a function of the dimensionless matrix stiffness, η, determined by combining either eqn (7)‖ or (8) and (10). Using either the full version of K from eqn (7) or its slender rod limit from eqn (8), provide nearly identical predictions (solid lines and dashed lines, respectively) within the range of dimensionless matrix stiffness explored in this study. In Fig. 3B, the theoretical prediction for λ (black dashed line) is also superposed on top of our experimental results discussed above, showing excellent quantitative agreement.

In summary, our linear stability analysis is therefore able to correctly predict the experimentally observed buckling wavelength. Moreover, eqn (6) indicates that, for certain values of k, two eigenmodes can be triggered simultaneously at the buckling onset, suggesting that the formation of non-planar buckling modes results from their interaction. This stability analysis is, however, unable to provide information on how these modes grow and interact. We now gain further insight into both of these effects through numerical simulations.

4 Numerical simulations

4.1 Discrete elastic rod simulations

We performed dynamic rod simulations using a code developed by Bergou *et al.*,[29] where the response of an extensible Kirchhoff rod[30,31] under external forces is computed using a symplectic Euler method to update the position of the discretized system. More details on the code can be found in the original paper.[29]

In our simulations, we matched the geometric and materials properties of the experimental Nitionol rods ($E_{\rm r} = 64$ GPa, $r_{\rm r} = 50$ μm and $L_{\rm r} = 9.7$ cm), with free rotation at both ends. Following the simplifications introduced in the theoretical description of Section 3, we modeled the confinement provided by the matrix as a series of linear springs with stiffness K given by eqn (8), acting in the radial direction. A total of 22 rods were simulated, with different values of K; the exact value of the parameters for each analysis is provided in Table S2 of the ESI.†

In Fig. 5A and B we present two representative simulated buckling configurations for $k = KL^4/(\pi E_{\rm r}I_{\rm r}) = 2450$ and 1764, respectively. For the case of $k = 2450$, our analytical model from Section 3 predicts that the compressive forces associated with the first and second eigenmodes are well separated (see eqn (6) and Fig. 4), which is consistent with the numerical finding that the rod buckles into a 2D planar configuration (Fig. 5A). By contrast, for $k = 1764$, eqn (6) is satisfied with $m = 6$, such that the critical buckling forces associated with modes 6 and 7 are the lowest and identical. In this case, theory predicts that the rod should buckle into a non-planar 3D configuration. This is corroborated by the numerical configuration in Fig. 5B where modes 6 and 7 are triggered almost simultaneously and grow in two perpendicular lateral directions. We note that the rods that buckle into planar configurations may eventually deform into non-planar shapes because of a second bifurcation.[32,33] However, this transition occurs at strains much higher than

‖ The buckling wavelength λ associated to eqn (7) has been calculated following a similar procedure to that reported above – see ESI for details.

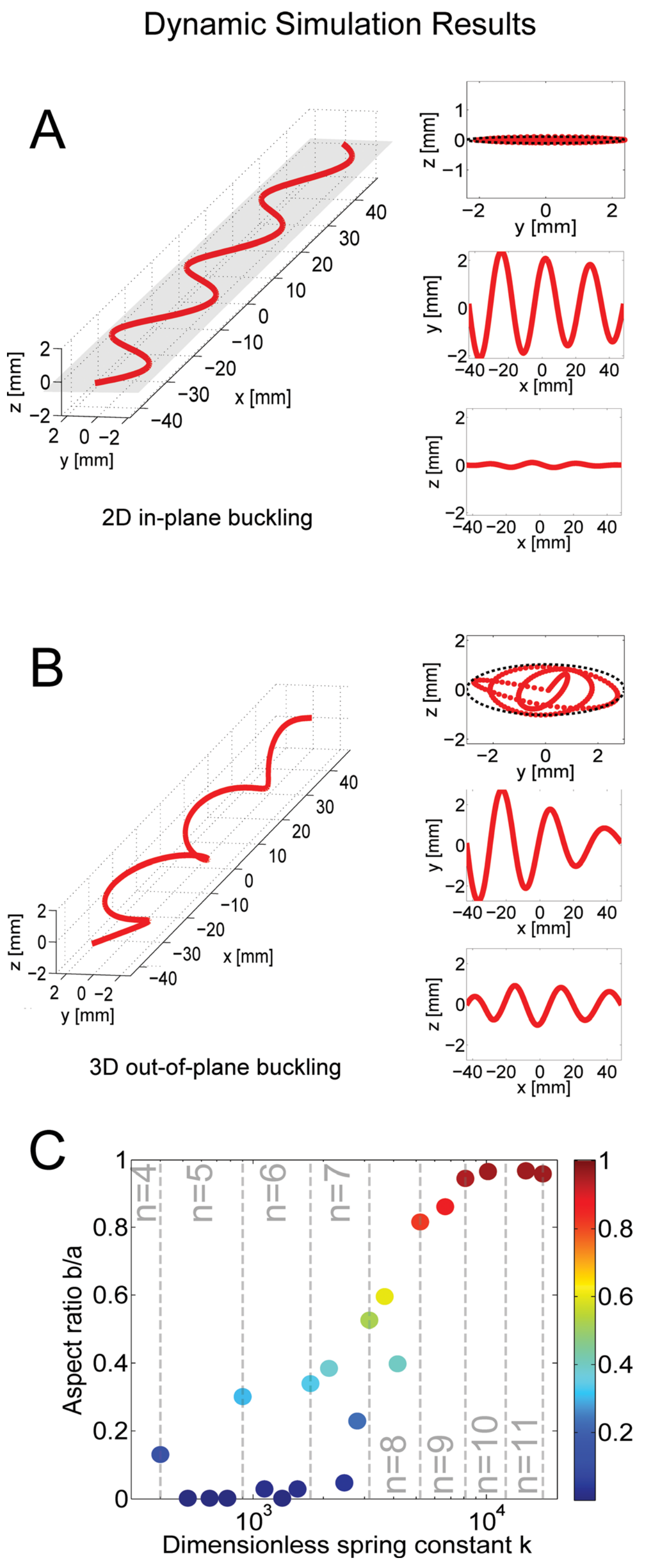

Fig. 5 Discrete elastic rod simulations. (A and B) Buckling configurations for (A) $k = 2450$, and (B) $k = 1764$. (C) Ratio between the minor and major axes b/a of the minimum area ellipse that encloses the rod cross sectional view as a function of dimensionless spring constant k. The critical $k = m^2(m+1)^2$ where two modes are expected to occur simultaneously are shown in vertical lines.

those associated to the onset of the first instability, and is therefore beyond the scope of our study.

Similarly to the analysis of the experimental results discussed in Section 2, for each simulated configuration, we have also computed the ellipse of minimum area that encloses the cross-sectional projection of the rod. In Fig. 5C we present the aspect ratio of this ellipse, b/a, as a function of the dimensionless spring constant k. For high values of the matrix stiffness ($k > 5000$), we find that $b/a \sim 1$ and the rod buckles in a non-planar configuration. On the other hand, for more moderate confinements ($k < 5000$), there is an alternation of 2D ($b/a \sim 0$) and 3D configurations as k is increased. These numerical findings are in good agreement with the experimental results presented earlier in Fig. 2.

These dynamic simulations agree qualitatively with the experiments of Section 2, and support the stability analysis and subsequent interpretation presented in Section 3: the formation of 3D buckling configuration is due to the interactions between eigenmodes that are triggered nearly simultaneously. It is important to note, however, that in these dynamic simulations, similarly to the analytical model in Section 3, we have made the simplifying assumption that the elastomeric matrix is modeled as an array of linear springs that only act in the radial direction. In doing so, we have completely neglected the effect of shear of the distorted matrix, which we shall now see through finite element analysis becomes important past the onset of the buckling instability.

4.2 Finite element simulations

In order to more accurately capture the effect of the deformation of the elastomeric matrix on the response of the rod, we have performed finite element (FE) simulations of our system using the commercial package Abaqus. In these analyses the matrix was discretized using brick elements (Abaqus element type C3D8R) and, because of the small strains considered in this study, was modeled as a linear elastic material with Poisson's ratio $\nu_m = 0.495$. The rod was modeled as a beam (Abaqus element type B31) and assumed to be perfectly bonded to the matrix (using the embedded element algorithm available in Abaqus). The accuracy of the mesh was ascertained through a mesh refinement study, resulting in 11 700 elements for the elastomeric matrix and 194 elements for the rod. In all FE simulations, we considered a rod with Young's modulus $E_r = 59$ GPa, radius $r_r = 101.5$ μm, length $L_r = 9.7$ cm and both ends were free to rotate. Moreover, the diameter of the matrix cylinder was chosen to be 2 cm, which was found to be sufficient to eliminate any boundary effects.

First, a buckling analysis was performed using a linear perturbation algorithm (through the BUCKLE module in Abaqus). We carried out 50 simulations with the dimensionless matrix stiffness in the range $(0.54 < \eta < 2.69)\ 10^5$ to investigate its effects on the stability of the rod. In Fig. 6A we report the normalized separation between the lowest two critical forces, $\Delta f/f_{cr}$, as a function of η, where the FE results (blue continuous line) are compared with the previous analytical prediction (red dashed line). The corresponding dimensionless spring

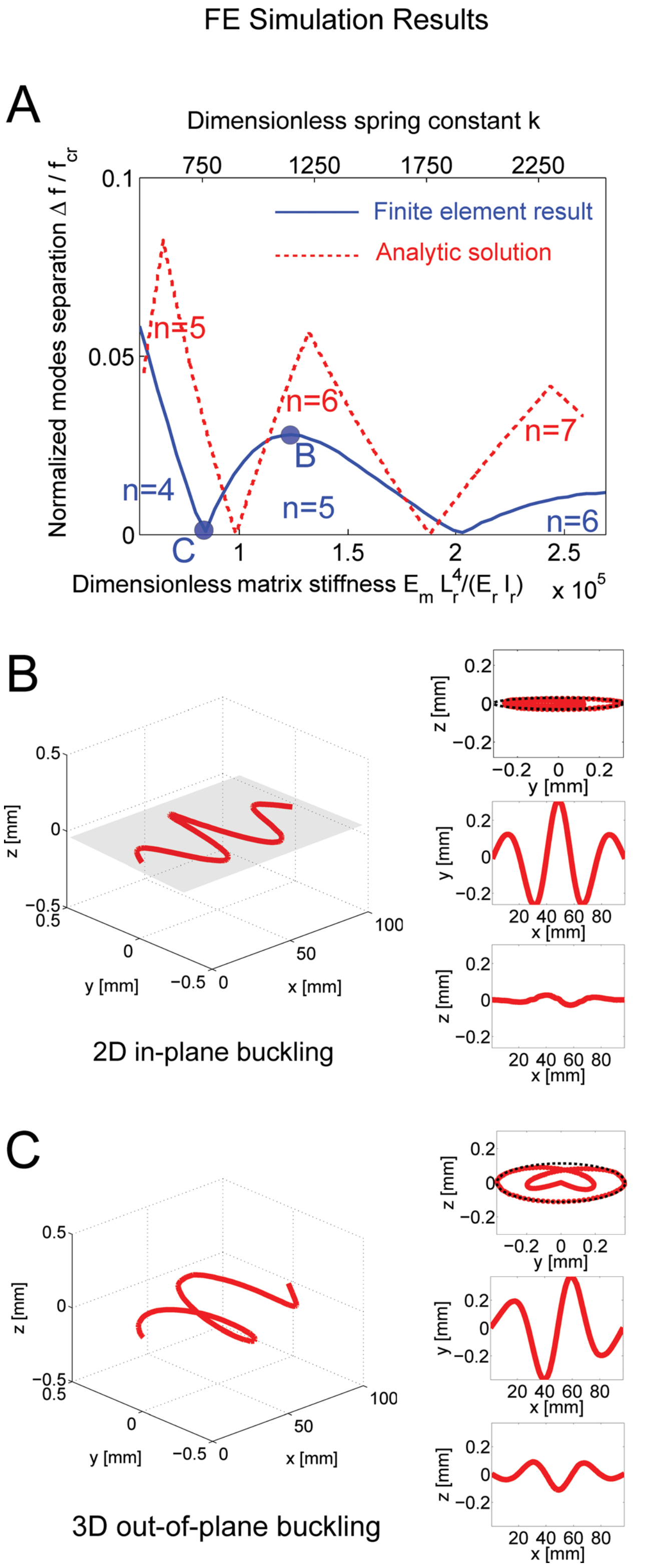

Fig. 6 Finite element (FE) results. (A) Normalized separation of the critical forces associated with the two lowest modes, $\Delta f/f_{cr}$, as a function of k (bottom) and the dimensionless matrix stiffness η (top) predicted by the theory (red line) and FE simulations (blue line). (B and C) Configurations recorded immediately after the buckling onset for systems with $\eta = 1.30 \times 10^5$ and 8.40×10^4, corresponding to markers B and C in (A).

constant, k, calculated using eqn (7) is also quantified on the upper horizontal axis. Both numerical and analytical results show the expected alternations of maxima and minima. However, there is a clear horizontal shift between the two sets of data. For example, in the region where theory predicts $n = 5$, we find $n = 4$ in the numerics and likewise for higher modes. This discrepancy indicates that although the simple Winkler foundation description does successfully provide a qualitative description of the response of the system, it is not sufficiently accurate to predict the exact conditions for which the rod will buckle into a 2D or 3D configuration. We speculate that the reasons for the differences between the reduced model (used in the analytical and the dynamic simulations) and the FE results is due to shear deformation in the matrix, which the Wrinkler model does not take into account.

Next, the post-buckling response was captured through dynamic explicit simulations, which were performed under quasi-static conditions ensured by monitoring the kinetic energy. In Fig. 6B and C we show two representative configurations recorded immediately after the buckling onset for two values of the dimensionless matrix stiffness $\eta = 1.30 \times 10^5$ and 8.40×10^4 (each marked in Fig. 6A by the points B and C, respectively). For $\eta = 1.30 \times 10^5$ a 2D buckling configuration is observed, as expected given that $\Delta f/f_{cr}$ is large in this case. In contrast, for $\eta = 8.40 \times 10^4$ a clear 3D buckling pattern emerges as the result of the interaction between two eigenmodes triggered nearly simultaneously, which grow in perpendicular directions. These FE results provide further confirmation that the dimensionless matrix stiffness determines whether the confined rod buckles into a 2D or 3D configuration by controlling the separation between the critical forces associated with the two lowest eigenmodes.

5 Discussion and conclusions

We have shown through a combination of experiments, theoretical analyses and numerical simulations that an elastic rod embedded within an elastomeric matrix can buckle into either a planar wavy configuration or a non-planar coiled configuration. Our analytical and numerical studies indicate that the separation $\Delta f/f_{cr}$ between the two lowest critical forces dictates the post-buckling behavior of the rod and that this parameter can be effectively controlled by changing the ratio between the stiffness of the matrix and the bending stiffness of the rod (*i.e.* the dimensionless matrix stiffness $\eta = E_m L_r^4/E_r I_r$). For large values of η the rod always buckles into a 3D coiled configuration, whereas for soft matrices, a monotonic increase of the stiffness results in an alternation between 2D planar and 3D coiled buckling configurations.

Good qualitative agreement was found between our analysis and experiments. However, a direct quantitative comparison is challenging due to the important role played by imperfections and measurement uncertainties. In fact, our analysis indicates that $\Delta f/f_{cr}$ is extremely sensitive to imperfections. For example, for a rod with $E_r = 59$ GPa, $L_r = 4$ cm, $r_r = 101.5$ µm embedded in a matrix with $E_m = 1.3$ kPa a relative uncertainty in the measurement of rod length and rod radius as small as 5%

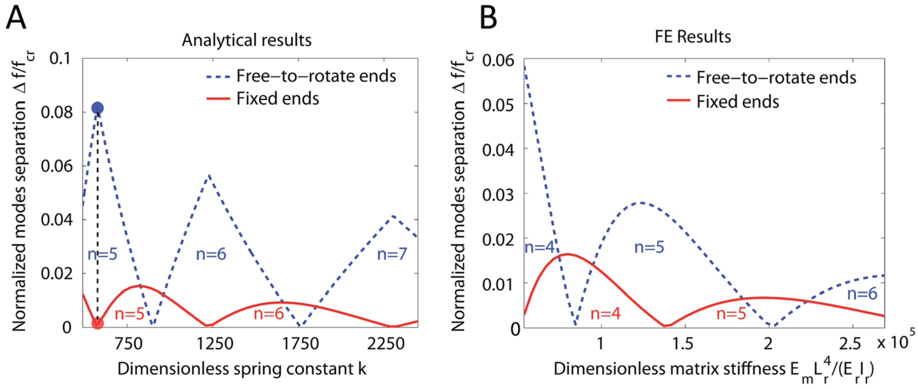

Fig. 7 Effect of boundary conditions. (A) Analytical predictions for the normalized separation of the critical forces associated with the two lowest modes, $\Delta f/f_{cr}$, as function of k for a rod with free-to-rotate (blue line) and fixed (red line) ends. (B) FE predictions for the normalized separation of the critical forces associated with the two lowest modes, $\Delta f/f_{cr}$, as function of η for a rod with free-to-rotate (blue line) and fixed (red line) ends.

(*i.e.* $\Delta L_r/L_r \leq 5\%$ and $\Delta r_r/r_r \leq 5\%$) modifies the prediction of $\Delta f/f_{cr}$ from 0.28 to 0.021, leading to a switch from a 2D to a 3D buckling configuration.

Furthermore, we have also found that the buckling pattern is highly sensitive to the boundary conditions imposed at the two ends of the rod. In the experiments, small segments of the rod near its ends were embedded into a much stiffer disk to provide support and minimize rotation. In analysis and simulations, however, we assumed for the sake of simplicity that both ends of the rod were free to rotate.

To address this issue on the important role of the boundary conditions, we have repeated the stability analysis presented in Section 3 and the FE simulations in Section 4.2, but now also for rods whose ends are fixed (see ESI for details†). In Fig. 7A and B we present analytical and numerical (FE) results, respectively, for the evolution of the normalized separation between the two lowest critical forces as a function of the dimensionless matrix stiffness and compare the two cases of a rod with fixed and free-to-rotate ends. Both sets of results indicate that the profile of $\Delta f/f_{cr}$ for the case of a rod with fixed ends is shifted by approximately half a zone compared to that corresponding to a rod with free-to-rotate ends. By way of example, for a dimensionless stiffness of $k = 576$, our theory predicts that a confined rod buckles into a non-planar configuration if its ends are fixed, but into a planar configuration if the ends are free to rotate. Moreover, for the rod with fixed ends, the peaks of $\Delta f/f_{cr}$ are lower in magnitude and decreases considerably faster as a function of k, indicating a greater tendency to buckle into a 3D coiled shape, when compared to the rod with free-to-rotate ends. These results demonstrate that the boundary conditions at the extremities of the rod play an important role in determining the buckling shape. If the boundary conditions are not perfectly fixed in the experiments, we expect these uncertainties to have a significant influence on the final buckled configuration.

In conclusion, we have demonstrated that a rod embedded in an elastomeric matrix can buckle either into a planar (2D) or a non-planar (3D) configuration, in a way that depends non-trivially on the geometric and material parameters, as well as the boundary conditions. The 3D buckling configurations were rationalized to arise when two eigenmodes are triggered nearly simultaneously. Furthermore, our analysis indicate that the buckling pattern can be controlled by tuning both the matrix stiffness and the boundary conditions. This tunability, combined with the scalability of the buckling phenomenon, opens avenues for exploiting the underlying mechanical instabilities to generate the next generation of future photonic and piezoelectric devices with complex 3D structure. However, given the sensitivity of the system to imperfections, our study calls for more accurate fabrication protocols and experimental procedures to be able to exploit buckling as mechanism to generate complex patterns with fine tunable features.

Acknowledgements

We thank Eitan Grinspun and Da Fang for their help in setting up the rod dynamic simulations and Jibo Wen for the help with preliminary experiments. D.T. thanks the Belgian American Education Foundation (B.A.E.F.), the Fulbright Program and the Wallonie-Bruxelles International Excellence Grant WBI.-World. P.M.R. acknowledges financial support from the National Science Foundation (CMMI-1129894).

References

1 J. Lankford, *J. Mater. Sci.*, 1995, **30**, 4343–4348.
2 C. Bower, R. Rosen, L. Jin, J. Han and O. Zhou, *Appl. Phys. Lett.*, 1999, **74**, 3317.
3 R. Parnes and A. Chiskis, *J. Mech. Phys. Solids*, 2002, **50**, 855–879.
4 M. Das, A. J. Levine and F. C. MacKintosh, *Europhys. Lett.*, 2008, **84**, 18003.
5 C. P. Brangwynne, F. C. MacKintosh, S. Kumar, N. A. Geisse, J. Talbot, L. Mahadevan, K. K. Parker, D. E. Ingber and D. A. Weitz, *J. Cell Biol.*, 2006, **173**, 733–741.
6 L. R. Herrmann, W. E. Mason and S. T. K. Chan, *J. Compos. Mater.*, 1967, **1**, 212–226.
7 Y. Lanir and Y. C. B. Fung, *J. Compos. Mater.*, 1972, **6**, 387–401.

8 Y. Li, N. Kaynia, S. Rudykh and M. C. Boyce, *Adv. Eng. Mater.*, 2013, **15**, 921–926.
9 T. C. Maltby and C. R. Calladine, *Int. J. Mech. Sci.*, 1995, **37**, 943–963.
10 T. C. Maltby and C. R. Calladine, *Int. J. Mech. Sci.*, 1995, **37**, 965–983.
11 J. L. Silverberg, R. D. Noar, M. S. Packer, M. J. Harrison, C. L. Henley, I. Cohen and S. J. Gerbode, *Proc. Natl. Acad. Sci. U. S. A.*, 2013, **109**, 16794–16799.
12 W. S. Klug, M. T. Feldmann and M. Ortiz, *Comput. Mech.*, 2005, **35**, 146–152.
13 P. R. Paslay and D. B. Bogy, *J. Appl. Mech.*, 1964, **31**, 605–610.
14 T. Su, N. Wicks, J. Pabon and K. Bertoldi, *Int. J. Solids Struct.*, 2013, **50**, 2468–2476.
15 F. Xu, W. Lu and Y. Zhu, *ACS Nano*, 2011, **5**, 672–678.
16 X. Y. Kong and Z. L. Wang, *Nano Lett.*, 2003, **3**, 1625–1631.
17 X. Chen, S. Zhang, D. A. Dikin, W. Ding, R. S. Ruoff, L. Pan and Y. Nakayama, *Nano Lett.*, 2003, **3**, 1299–1304.
18 M. A. Poggi, J. S. Boyles, L. A. Bottomley, A. W. McFarland, J. S. Colton, C. V. Nguyen, R. M. Stevens and P. T. Lillehei, *Nano Lett.*, 2004, **4**, 1009–1016.
19 S. P. Timoshenko and J. M. Gere, *Theory of Elastic Stability*, McGraw-Hill, 2nd edn, 1961.
20 D. C. Lagoudas, *Shape Memory Alloys: Modeling and Engineering Applications*, Springer, 2010.
21 D. Stoeckel and W. Yu, *Wire J. Int.*, 1991, **24**, 45–50.
22 F. Brau, H. Vandeparre, A. Sabbah, C. Poulard, A. Boudaoud and P. Damman, *Nat. Phys.*, 2011, **7**, 56–60.
23 W. Shan, Z. Chen, C. P. Broedersz, A. A. Gumaste, W. O. Soboyejo and C. P. Brangwynne, *Soft Matter*, 2013, **9**, 149–199.
24 I. T. Jolliffe, *Principal Component Analysis*, Springer, 2nd edn, 2002.
25 M. Ringnér, *Nat. Biotechnol.*, 2008, **28**, 303–304.
26 H. Jiang and J. Zhang, *J. Appl. Mech.*, 2008, **75**, 061019.
27 J. Wu, Z. J. Liu, J. Z. Song, Y. Huang, K.-C. Hwang, Y. W. Zhang and J. A. Rogers, *Appl. Phys. Lett.*, 2011, **99**, 61911.
28 E. Byskov and J. W. Hutchinson, *AIAA J.*, 1977, **15**, 941–948.
29 M. Bergou, M. Wardetzky, S. Robinson, B. Audoly and E. Grinspun, *ACM Transactions on Graphics*, 2008, **27**, 63.
30 G. Kirchhoff, *J. Reine Angew. Math.*, 1859, **56**, 285–313.
31 G. Kirchhoff, *Vorlesungen über mathematische Physik: Mechanik*, 1876.
32 G. H. M. Van der Heijden, S. Neukirch, V. G. A. Goss and J. M. T. Thompson, *Int. J. Mech. Sci.*, 2003, **45**, 161–196.
33 S. Goyal, N. C. Perkins and C. L. Lee, *J. Comput. Phys.*, 2005, **209**, 371–389.

Supplementary Material for the article "Alternation between planar and coiled modes in slender rods embedded in soft elastic matrices"

Tianxiang Su[a,†], Jia Liu[a,†], Denis Terwagne[b,c,†], Pedro M. Reis[*,b,d], and Katia Bertoldi[*,a,e]

[a] *School of Engineering and Applied Sciences, Harvard University, Cambridge, MA, 02138, USA*
[b] *Department of Civil and Environmental Engineering, Massachusetts Institute of Technology, Cambridge, MA, 02139, USA*
[c] *Current address: Faculté des Sciences, Université Libre de Bruxelles (ULB), Bruxelles 1050, Belgium*
[d] *Department of Mechanical Engineering, Massachusetts Institute of Technology, Cambridge, MA, 02139, USA*
[e] *Kavli Institute for Bionano Science and Technology, Harvard University, Cambridge, MA, 02138, USA*
[†] *These authors contributed equally to this work.*
[*] *To whom correspondence may be addressed. E-mail: preis@mit.edu and bertoldi@seas.harvard.edu*

S1 Experiment setup

Fabricating matrices with different stiffness

For the fabrication of the elastomeric matrix surrounding the Nitinol rod, we used PDMS (Sylgard 184 from Dow Corning Inc.). This product comes in two parts, a curing agent and a base agent, that we have to mix prior curing. Curing of the PDMS was performed using a convection oven at a low temperature of $T = 40\,^\circ$C for 24 hours ensuring a negligible thermal dilatation of the molds and PDMS and thus stress free samples after curing. The Dow Corning recommandation is to use a base/cure ratio in weight of 10:1, which produce an elastomer of Young modulus of 2100 kPa after curing. By varying the base/cure ratio from 80:1 to 10:1 and thus changing the amount of cross linkers, one can vary the Young modulus of the elastomeric sample, typically from 1 kPa to 2.1 MPa.

To measure the elastic modulus, we casted a small cylinder sample (2 cm long and 2.6 cm in diameter) along with each PDMS matrix using the same mixture and protocol. These small cylinders were then tested under compression using a Zwick material testing machine. By importing the displacement and force measurements and using a linear elastic model, we deduced the Young modulus for each or the elastomeric matrices. Due to the geometry of our test, i.e. the barreling of the sample cylinder when compressed, a correction factor on the inferred Young modulus had to be taken into account [1]. These measurements of the elastic modulus as a function of ratio base/cure agent are represented on Fig. S1 along with other results taken from the literature [2, 3, 4, 5].

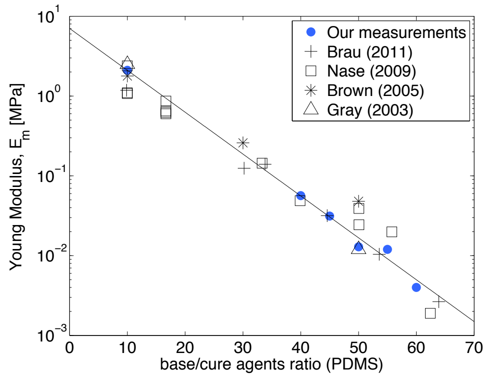

Figure S1: Elastic modulus of Polydimethylsiloxane Dow Corning Sylgard 184 as a function of the ratio of base agent on cure agent. Measurements on our samples are represented using full disk symbol along with other measurements form the literature [2, 3, 4, 5].

Sample parameters

We made a total of 15 samples in this study. The parameters for all the samples and their cross-sectional buckling shapes at compressive strain $\epsilon = 3\%$ are shown in Tab. S1.

Table S1: Parameters characterizing all the 15 samples. d_r is diameter of the rod; E_r is the Young's modulus of the rod; E_m is the Young's modulus of the matrix; L_r is the length of the rod; $\delta_{\max}$ is the maximum applied displacement during the test; $E_m L_r^4/(E_r I_r)$ is the dimensionless matrix stiffness, $I_r = \pi d_r^4/64$ being the second moment of inertia of the rod cross section. In the last column a cross sectional view of the buckled sample at $\epsilon = 3\%$ is shown.

Name	d_r [μm]	E_r [GPa]	E_m [kPa]	L_r [m]	$\delta_{\max}$ [mm]	$E_m L_r^4/E_r I_r$ [10^6]	Buckled shape $\epsilon = 3\%$
S26	203	59.23 ± 0.07	32.59 ± 0.69	0.041	2	0.0190	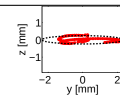
S25	254	67.01 ± 0.69	32.59 ± 0.69	0.055	2.5	0.0213	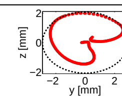
S15	254	67.01 ± 0.69	29.45 ± 0.50	0.097	4	0.19	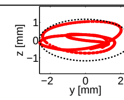
S24	203	59.23 ± 0.07	13.85 ± 0.33	0.098	5	0.26	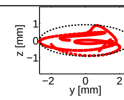
S8	254	67.01 ± 0.69	66.73 ± 0.96	0.099	5	0.47	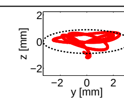
S17	203	59.23 ± 0.07	32.85 ± 0.54	0.097	3	0.59	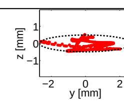
S23	152	67.95 ± 0.77	13.85 ± 0.33	0.097	7	0.69	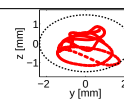
S21	203	59.23 ± 0.07	49.63 ± 0.67	0.097	4	0.89	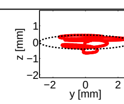
S14	152	67.95 ± 0.77	29.45 ± 0.50	0.097	4	1.46	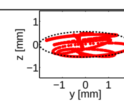
S7	152	67.95 ± 0.77	59.96 ± 0.78	0.094	4	2.63	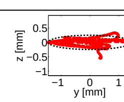
S22	100	64.24 ± 0.24	13.85 ± 0.33	0.097	9	3.89	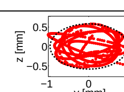
S16	100	64.24 ± 0.24	32.85 ± 0.54	0.097	9	9.22	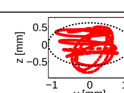
S20	100	64.24 ± 0.24	49.63 ± 0.67	0.097	6	13.93	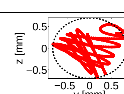
S18	50.8	60.93 ± 1.26	10.05 ± 0.32	0.097	5	44.68	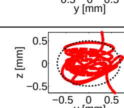
S13	50.8	60.93 ± 1.26	29.45 ± 0.50	0.097	5	130.87	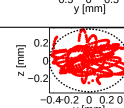

S2 Computing the minimum area ellipse that encloses the cross-sectional view of the buckled rod

To better characterize the buckling shape, for each sample we computed the minimum area ellipse that encloses the cross-sectional view of the buckled rod at a given level of applied compressive strain ϵ. First, to facilitate the analysis, we rigidly rotated the rod using Principal Component Analysis (PCA) [6, 7] and aligned the major lateral buckling direction with the y axis (the matrix central axis was aligned with x). Then, we focused on the lateral $y - z$ plane and computed the ellipse with the smallest possible area that encloses all points $[y_i, z_i]$ along the rod (note that to eliminate boundary effects, we only focused on points of the rod away from the boundaries and neglected those within 1/6 of its length from both ends). Therefore, denoting with a and b the major and minor axes of the ellipse, we required

$$\frac{y_i^2}{a^2} + \frac{z_i^2}{b^2} \leq 1, \quad \text{for all } \ i = 1, 2, 3, \cdots N \tag{S1}$$

so that

$$a^2 \geq \max_i \left(\frac{y_i^2}{1 - z_i^2/b^2} \right). \tag{S2}$$

Therefore, for a given a value of b the lower bound for the area of the ellipse $S = \pi\, a\, b$ was obtained as

$$S = \pi a b \geq \max_i \left(\frac{\pi y_i}{\sqrt{1/b^2 - z_i^2/b^4}} \right). \tag{S3}$$

Finally, we determined numerically the minor axis b that minimizes the area,

$$S_{\min} = \min_b \left[\max_i \left(\frac{\pi y_i}{\sqrt{1/b^2 - z_i^2/b^4}} \right) \right]. \tag{S4}$$

Two examples of minimum area ellipses (black dashed line) obtained for samples #7 and #18 together with the trace of rod coordinates (red line) are shown in Fig. S2A and B . Note that the aspect ratio of the ellipse (*i.e.*, the ratio between the minor and major axes b/a) characterizes whether the buckling shape is 2D or 3D: A flat ellipse with a small b/a value indicates an in-plane buckling shape, while a more circular one with $b/a \to 1$ indicates a 3D buckling shape.

S3 Buckling analysis using the Winkler foundation model

While in the main text we focus on the results of the buckling analysis, here we present the details of the analysis.

To understand and quantify the conditions leading to 2D and 3D buckling configurations, we adopt the Winkler foundation model and simplify the matrix as an array of springs with stiffness K acting only in radial direction. Consequently, assuming small strain and moderate rotation, the governing equation for the embedded elastic rod is given by

$$E_r I_r \frac{\partial^4 Y}{\partial S^4} + F \frac{\partial^2 Y}{\partial S^2} + K\, Y = 0, \tag{S5}$$

where $E_r I_r$ is the bending stiffness of the rod, F is the applied compressive force and Y and S denote the lateral displacement and the arc length of the rod, respectively. By introducing

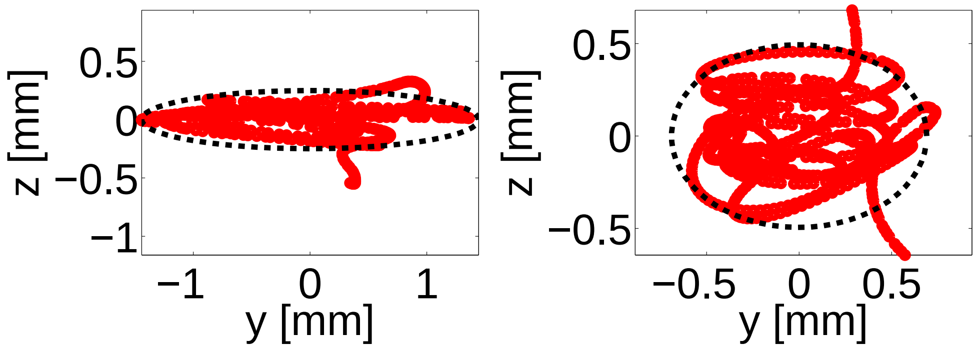

Figure S2: Two examples of minimum area ellipses (dashed black lines) that enclose the cross-sectional view of the buckled rod (red traces).

the normalized displacement, $y = Y/L_r$, and arc length, $s = S/L_r$, Eq. (S5) can be rewritten in dimensionless form as

$$\frac{\partial^4 y}{\partial s^4} + \pi^2 f \frac{\partial^2 y}{\partial s^2} + \pi^4 k\, y = 0, \tag{S6}$$

where $f = FL_r^2/(\pi^2 E_r I_r)$ and $k = K\, L_r^4/(\pi^4 E_r I_r)$ are the dimensionless compressive force and spring constant, respectively.

To solve for the critical force f_{cr}, one needs to specify boundary conditions. Here, we consider two types of boundary conditions: (*Case A*) both ends are free to rotate; (*Case B*) both ends are fixed.

Case A: Both ends are free-to-rotate

When both ends of the rod are free to rotate,

$$y(0) = y(1) = 0,\ y''(0) = y''(1) = 0 \tag{S7}$$

where $(\cdot)' = \partial(\cdot)/\partial s$. For this case, the solution of Eq. (S6) takes the form

$$y(s) = A\,\sin(n\pi s), \tag{S8}$$

where n is an integer. Substitution of Eq. (S8) into Eq. (S6) yields

$$A\,n^4\pi^4 \sin(n\pi s) - An^2\pi^4 f \sin(n\pi s) + A\pi^4 k \sin(n\pi s) = 0, \tag{S9}$$

which can be simplified as

$$n^4 - n^2 f + k = 0. \tag{S10}$$

Therefore, non-trivial solutions to Eq. (S6) exist when

$$f = f_n = \frac{k + n^4}{n^2}, \tag{S11}$$

where f_n denotes the compressive force f_n required to trigger the n-th mode. Since during loading the mode associated to the lowest f_n emerges and grows, the critical buckling force for the system is given by

$$f_{\rm cr} = \min_{n=1,2,\cdots} \left(n^2 + \frac{k}{n^2} \right). \tag{S12}$$

Case B: both ends are fixed

When both ends of the rod are fixed

$$y(0) = y(1) = 0, \; y'(0) = y'(1) = 0, \tag{S13}$$

and the form of solution to Eq. (S6) is found by examining the roots of its characteristic equation

$$x^4 + \pi^2 f\, x^2 + \pi^4 k = 0. \tag{S14}$$

Note that the form of the solution depends on the sign of $f^2 - 4k$.

1. For $f^2 - 4k > 0$, Eq. (S14) has four imaginary roots,

$$\alpha = \pm \frac{i\pi}{\sqrt{2}} \sqrt{f + \sqrt{f^2 - 4k}}, \qquad \beta = \pm \frac{i\pi}{\sqrt{2}} \sqrt{f - \sqrt{f^2 - 4k}}. \tag{S15}$$

   Therefore, the general solution to Eq. (S6) is given by

$$y(s) = A_1 \sin(\alpha s) + A_2 \cos(\alpha s) + A_3 \sin(\beta s) + A_4 \cos(\beta s), \tag{S16}$$

   so that

$$y'(s) = A_1 \alpha \cos(\alpha s) - A_2 \alpha \sin(\alpha s) + A_3 \beta \cos(\beta s) - A_4 \beta \sin(\beta s) \tag{S17}$$

   where A_1, A_2, A_3, A_4 are arbitrary constants which are determined by imposing the boundary conditions. Substitution of Eqs. (S16) and (S17) into the boundary conditions (S13), yields

$$\begin{aligned} & A_2 + A_4 = 0 \\ & A_1 \alpha + A_3 \beta = 0 \\ & A_1 \sin(\alpha) + A_2 \cos(\alpha) + A_3 \sin(\beta) + A_4 \cos(\beta) = 0 \\ & A_1 \alpha \cos(\alpha) - A_2 \alpha \sin(\alpha) + A_3 \beta \cos(\beta) - A_4 \beta \sin(\beta) = 0 \end{aligned} \tag{S18}$$

   which can be written as $\mathbf{K}\mathbf{a} = \mathbf{0}$, where $\mathbf{K}$ is a coefficient matrix and $\mathbf{a} = (A_1, A_2, A_3, A_4)^T$. Generally, the matrix $\mathbf{K}$ is not singular and only the trivial solution $\mathbf{a} = \mathbf{0}$ exists. However, for certain values of f, $\mathbf{K}$ becomes singular (i.e. $\det(\mathbf{K}) = 0$) and in that case a non-zero solution is found, indicating the occurrence of buckling. Note that in this case explicit formulae for the critical force cannot be obtained and buckling is detected numerically by finding the values of f for which $\det(\mathbf{K}) = 0$.

2. If $f^2 - 4k = 0$, the roots of Eq. (S14) are given by

$$\alpha = \pm i\, \pi k^{1/4}, \tag{S19}$$

   and the solution of Eq. (S6) takes the form

$$y(s) = A_1 \sin(\alpha s) + A_2 s \sin(\alpha s) + A_3 \cos(\alpha s) + A_4 s \cos(\alpha s), \tag{S20}$$

   so that

$$\begin{aligned} y'(s) = \; & A_1 \alpha \cos(\alpha s) + A_2 (\sin(\alpha s) + \alpha s \cos(\alpha s)) \\ & - A_3 \alpha \sin(\alpha s) + A_4 (\cos(\alpha s) - \alpha s \sin(\alpha s)) \end{aligned} \tag{S21}$$

Substitution of Eqs. (S20) and (S21) into the boundary conditions (S13), yields

$$\begin{aligned}
&A_3 = 0 \\
&A_1\alpha + A_4 = 0 \\
&A_1\sin(\alpha) + A_2\sin(\alpha) + A_3\cos(\alpha) + A_4\cos(\alpha) = 0 \\
&A_1\alpha\cos(\alpha) + A_2(\sin(\alpha) + \alpha\cos(\alpha)) \\
&-A_3\alpha\sin(\alpha) + A_4(\cos(\alpha) - \alpha\sin(\alpha)) = 0
\end{aligned} \tag{S22}$$

which admit only trivial solution $\mathbf{a} = \mathbf{0}$, since f in this case has a fixed value (i.e. $f = 2\sqrt{k}$) and cannot vary.

3. For $f^2 - 4k < 0$, Eq. (S14) has four complex roots

$$\alpha = \pi k^{1/4}\left(\pm\cos\theta \pm i\sin\theta\right), \tag{S23}$$

where

$$\theta = \frac{1}{2}\left[\pi - \arcsin\left(\sqrt{1 - \frac{f^2}{4k}}\right)\right] \tag{S24}$$

. Therefore, the general solution of Eq. (S6) has the form

$$\begin{aligned}
y(s) = \; & A_1\exp(\gamma s)\sin(\beta s) + A_2\exp(\gamma s)\cos(\beta s) \\
& + A_3\exp(-\gamma s)\sin(\beta s) + A_4\exp(-\gamma s)\cos(\beta s),
\end{aligned} \tag{S25}$$

so that

$$\begin{aligned}
y'(s) = \; & A_1\exp(\gamma s)(\gamma\sin(\beta s) + \beta\cos(\beta s)) + A_2\exp(\gamma s)(\gamma\cos(\beta s) - \beta\sin(\beta s)) \\
& + A_3\exp(-\gamma s)(-\gamma\sin(\beta s) + \beta\cos(\beta s)) - A_4\exp(-\gamma s)(\gamma\cos(\beta s) + \beta\sin(\beta s)),
\end{aligned} \tag{S26}$$

where $\gamma = \pi k^{1/4}\cos\theta$ and $\beta = \pi k^{1/4}\sin\theta$. Finally, the boundary conditions require that

$$\begin{aligned}
&A_2 + A_4 = 0 \\
&A_1\beta + A_2\gamma + A_3\beta - A_4\gamma = 0 \\
&A_1\exp(\gamma)\sin(\beta) + A_2\exp(\gamma)\cos(\beta) + \\
&A_3\exp(-\gamma)\sin(\beta) + A_4\exp(-\gamma)\cos(\beta) = 0 \\
&A_1\exp(\gamma)(\gamma\sin(\beta) + \beta\cos(\beta)) + A_2\exp(\gamma)(\gamma\cos(\beta) - \beta\sin(\beta)) \\
&+A_3\exp(-\gamma)(-\gamma\sin(\beta) + \beta\cos(\beta)) + A_4\exp(-\gamma)(-\gamma\cos(\beta) - \beta\sin(\beta)) = 0,
\end{aligned} \tag{S27}$$

which can be rewritten as $\mathbf{Ka} = \mathbf{0}$, and the non-zero solution, if exists, is detected by setting $\det(\mathbf{K}) = 0$.

S4 Winkler foundation model: Relation between the spring stiffness K and the matrix shear modulus G_m

In our analysis we adopted the Winkler foundation model and simplified the matrix as an array of springs with stiffness K acting only in radial direction. Therefore, to make a connection between the prediction of the analytical model and the experimental results a relation between the spring stiffness K and the matrix shear modulus $G_m = E_m/[2(1+\nu_m)]$ needs to be established. For an elastic rod of radius r_r and length L_r buckled into mode n it has been shown that K is related to G_m and ν_m as [8, 9]

$$K = \frac{16\pi G_m(1-\nu_m)}{2(3-4\nu_m)K_0\left(n\pi\frac{r_r}{L_r}\right) + n\pi\frac{r_r}{L_r}K_1\left(n\pi\frac{r_r}{L_r}\right)}, \tag{S28}$$

where $K_0(\cdot)$ and $K_1(\cdot)$ are the modified bessel function of second kind.

It is worth noting that for slender rods, for which $r_r/L_r \to 0$, Eq. (S28) significantly simplifies, since

$$\lim_{r_r/L_r \to 0} n\pi \frac{r_r}{L_r} K_1\left(n\pi \frac{r_r}{L_r}\right) = 1 \tag{S29}$$

and

$$\lim_{r_r/L_r \to 0} K_0\left(n\pi \frac{r_r}{L_r}\right) = +\infty. \tag{S30}$$

Therefore, when $r_r/L_r \to 0$ the second term of the denominator in Eq. (S28) can be neglected, so that

$$K = \frac{16\pi G_m(1-\nu_m)}{2(3-4\nu_m)K_0\left(n\pi \frac{r_r}{L_r}\right)}, \tag{S31}$$

Furthermore, we note that for slender rods

$$\lim_{r_r/L_r \to 0} \frac{\ln\left(\frac{2L_r}{n\, r_r}\right)}{K_0\left(n\pi \frac{r_r}{L_r}\right)} = 1, \tag{S32}$$

and

$$\lim_{r_r/L_r \to 0} \ln\left(\frac{2L_r}{n\, r_r}\right) - K_0\left(n\pi \frac{r_r}{L_r}\right) = 1.72195, \tag{S33}$$

so that Eq. (S31) can be rewritten as

$$K = \frac{16\pi G_m(1-\nu_m)}{2(3-4\nu_m)\ln\left(\frac{2L_r}{n\, r_r}\right)} \qquad \text{when } r_r/L_r \to 0. \tag{S34}$$

Finally, for the case of rods embedded in soft, elastomeric matrices $\nu_m = 0.5$, so that

$$K = \frac{4\pi G_m}{\ln\left(\frac{2L_r}{n\, r_r}\right)} \qquad \text{when } r_r/L_r \to 0, \tag{S35}$$

which has been recently used to study buckling of confined microtubules [10].

S5 Relation between λ, K and G_m from Eq. (6)

Although both Eqs. (S28) and (S35) (corresponding to Eqs. (6) and (7) in the main text) indicate that the spring stiffness K depends not only on shear modulus of the matrix G_m, but also on the mode wavelength, $\lambda = 2L_r/n$, in the main text we showed for Eq. (7) that a unique relation between λ, G_m and K can be established by calculating the mode number that minimize the critical force f_n (i.e. calculating n for which $\partial f_n/\partial n = 0$). A similar procedure can be followed to determine the relation between λ, G_m and K also when Eq. (6) is used:

1. Eq. (6) is substituted into Eq. (3), yielding

$$f_n = n^2 + \frac{k}{n^2} = n^2 + \frac{E_m L_r^4}{E_r I_r} \cdot \frac{8}{3\pi^3} \cdot \frac{1}{n^2(2K_0(n\pi r_r/L_r) + n\pi r_r/L_r \cdot K_1(n\pi r_r/L_r))}, \tag{S36}$$

   where, for the sake of simplicity, we assume $\nu_m = 0.5$.

2. The mode number that minimize the critical force f_n is calculated by requiring $\partial f_n/\partial n = 0$,

$$2n - \frac{E_m L_r^4}{E_r I_r}\frac{8}{3\pi^3}\frac{n(2K_0'\pi r_r/L_r + \pi r_r/L_r K_1 + n\pi r_r/L_r K_1'\pi r_r/L_r) + 2(2K_0 + n\pi r_r/L_r K_1)}{n^3(2K_0 + n\pi r_r/L_r K_1)^2} = 0, \tag{S37}$$

where $K_0 = K_0(n\pi r_r/L_r)$ and $K_1 = K_1(n\pi r_r/L_r)$. Note that $n = 2L_r/\lambda$, so that Eq. (S37) can be rewritten in terms of λ as

$$\left(\frac{L_r}{\lambda}\right)^4 \frac{(K_0 + \pi r_r/\lambda \cdot K_1)^2}{L_r/r_r(2K_0'\pi r_r/L_r + K_1\pi r_r/L_r + 2\pi r_r/\lambda \cdot K_1' \cdot \pi r_r/L_r) + (2K_0 + 2\pi r_r/\lambda \cdot K_1)} = \frac{1}{24\pi^3}\frac{E_m L_r^4}{E_r I_r}, \tag{S38}$$

3. The wavelength λ is solved numerically from Eq. (S38);

4. Eq. (6) now provides a unique relation between K and G_m, since λ is known.

S6 An alternative approach for the buckling analysis: the energy approach

In the main text, we used the Winkler foundation model to study analytically the stability of a thin and stiff beam supported by a softer elastic substrate. Following this approach, the interaction between the rod and substrate is simplified as an array of springs with stiffness K acting solely in radial direction, so that the differential equation governing the problem can be easily established and directly solved. However, it is important to highlight the fact the stability analysis can be alternatively conducted by minimizing the total elastic energy of the system [11, 12, 13, 14]. In the following, we study the stability of a rod embedded in a softer matrix using the energy approach and demonstrate that this analysis yields the same results presented in the main text.

We start by constructing the total elastic energy of the system (per unit length), Π_{tot},

$$\Pi_{tot} = U_{bending} + U_{stretching} + U_{interaction}, \tag{S39}$$

where $U_{bending}$ and $U_{stretching}$ are the bending and stretching energy per unit length of the rod, respectively, and $U_{interaction}$ denotes the interaction energy between the substrate and the matrix energy per unit length. As typically done [11, 12, 13, 14], we choose the von Karman formulation to describe $U_{bending}$ and $U_{stretching}$. Therefore, denoting with ϵ the applied compressive strain and assuming the buckling mode to be described by a sinusoidal curve, $w = A\sin(n\pi x/L_r)$, we get

$$U_{bending} = \frac{1}{2L_r}E_r I_r \int_0^{L_r} (w'')^2 \mathrm{d}x = \frac{1}{4}E_r I_r A^2 \left(\frac{n\pi}{L_r}\right)^4, \tag{S40}$$

$$U_{stretching} = \frac{1}{2L_r}E_r S_r \int_0^{L_r} \left[u' + \frac{1}{2}(w')^2\right]^2 \mathrm{d}x = \frac{1}{2}E_r S_r \left[-\epsilon + \frac{1}{4}A^2\left(\frac{n\pi}{L_r}\right)^2\right]^2, \tag{S41}$$

where S_r is the cross-sectional area of the rod and u and w denote the axial and lateral components of its displacement, respectively.

Finally, we need to specify a form for the interaction energy between the rod and the matrix. Here, as for the Winkler foundation model, we simplified the matrix as an array of springs with stiffness K acting solely in radial direction, so that

$$U_{interaction} = \frac{1}{2L_r}\int_0^{L_r} K w^2 \mathrm{d}x = \frac{1}{4}K\,A^2. \tag{S42}$$

Note that the spring constant K is not an arbitrary constant. In fact, rigorous expressions for K have been established by modeling the matrix as infinite elastic solid, using the classic theory of elasticity and accounting for the radius of the rod [8].

To determine the critical force F_{cr}, we now substitute Eqs. (S40), (S41) and (S42) into Eq. (S39), and minimize Π_{tot} with respect to A, obtaining

$$\frac{1}{2}E_r I_r A\left(\frac{n\pi}{L_r}\right)^4 + \frac{1}{2}E_r S_r\left[-\epsilon + \frac{1}{4}A^2\left(\frac{n\pi}{L_r}\right)^2\right]A\left(\frac{n\pi}{L_r}\right)^2 + \frac{1}{2}K\,A = 0, \tag{S43}$$

from which the amplitude of the mode A can be solved as

$$A = \begin{cases} \sqrt{\dfrac{4L_r^4}{E_r S_r\,(n\pi)^4}\left[-K - E_r I_r\left(\dfrac{n\pi}{L_r}\right)^4 + E_r S_r \epsilon\left(\dfrac{n\pi}{L_r}\right)^2\right]}, & \text{if}\quad E_r S_r \epsilon\left(\dfrac{n\pi}{L_r}\right)^2 \geq K + E_r I_r\left(\dfrac{n\pi}{L_r}\right)^4, \\ 0, & \text{if}\quad E_r S_r \epsilon\left(\dfrac{n\pi}{L_r}\right)^2 < K + E_r I_r\left(\dfrac{n\pi}{L_r}\right)^4. \end{cases} \tag{S44}$$

The compressive strain required to trigger the n-th mode, ϵ_n, can be then obtained taking the limit for $A \to 0$ in (S44), yielding

$$\epsilon_n = \frac{I_r}{S_r}\left(\frac{n\pi}{L_r}\right)^2 + \frac{K}{E_r S_r}\left(\frac{L_r}{n\pi}\right)^2, \tag{S45}$$

so that the force required to trigger the n-th mode is given by

$$F_n = E_r S_r \epsilon_n = E_r I_r\left(\frac{n\pi}{L_r}\right)^2 + K\left(\frac{L_r}{n\pi}\right)^2. \tag{S46}$$

At this point we want to highlight the fact that, when normalized, the expression for the critical force given by Eq. (S46) is identical to that reported in Eq. (4) of the main text, confirming the fact that the stability analysis reported in the main text and the one based on the energy approach are equivalent.

The critical mode can then be determined upon calculation of the mode number n that minimizes F_n (*i.e.* determining the values of n for which $\partial F_n/\partial n = 0$). In particular, minimization of F_n using Eq. (S46) yields,

$$E_r I_r\left(\frac{n\pi}{L_r}\right)^2 - K\left(\frac{L_r}{n\pi}\right)^2 + \frac{1}{2}\frac{\partial K}{\partial n}\frac{L_r}{\pi} = 0, \tag{S47}$$

which reduces to the expression reported in Eq. (9) of the main text when the expression for K provided by Eq. (S35) is substituted in, further demonstrating that the energy approach converges to the exact same results obtained by solving directly the differential equations.

Finally, we want to highlight the fact that, although in literature different forms for the interaction energy $U_{interaction}$ have been used [11, 12, 13, 14], the reported results closely resemble those derived above. To demonstrate this important point, we follow Jiang et al. [13] and construct $U_{interaction}$ by superposition of a series of solutions for point loads in the (semi-) infinite 3D space [1], yielding

$$U_{interaction} = \frac{3\beta^2}{32\pi E_m}\left[3 - 2\gamma - 2\ln\left(\frac{n\pi r_r}{L_r}\right)\right], \tag{S48}$$

where $\gamma = 0.577$ is the Euler's constant and β is given by

$$\beta = -E_r I_r A\left(\frac{n\pi}{L_r}\right)^4 - E_r S_r\left[\frac{1}{4}A^2\left(\frac{n\pi}{L_r}\right)^2 - \epsilon\right] A\left(\frac{n\pi}{L_r}\right)^2. \tag{S49}$$

Substitution of Eq. (S48) into Eq. (S39), and minimization of Π_{tot} with respect to A results in the following prediction for the wave number n (see Eq. (32) in [13])

$$n\left(\frac{E_r I_r}{G_m}\right)^{1/4} = \left\{\frac{16\pi[1-\gamma-\ln(n\,r_r)]}{[3-2\gamma-2\ln(n\,r_r)]^2}\right\}^{1/4}, \tag{S50}$$

where $G_m = E_m/(2(1+\nu_m))$ is the initial shear modulus of the matrix. Noting for an incompressible matrix (i.e. $\nu_m = 0.5$)

$$G_m = \frac{E_m}{3}, \tag{S51}$$

and that

$$\ln(n\,r_r) = \ln(2\pi) - \ln(\lambda/r_r), \tag{S52}$$

$\lambda = 2\pi/n$ being the wavelength, Eq. (S50) can be rewritten as

$$\frac{(\lambda/L_r)^4[\ln(\lambda/r_r) + 1 - \gamma - \ln(2\pi)]}{[2\ln(\lambda/r_r) + 3 - 2\gamma - 2\ln(2\pi)]^2} = \frac{3\pi^3}{\eta}, \tag{S53}$$

where $\eta = (E_m L_r^4)/(E_r I_r)$ is the dimensionless matrix stiffness. Furthermore, as noted by the authors in [13], for a wide range of values of E_m Eq. (S53) can be simplified to

$$\frac{\lambda}{L_r} = 3^{1/4}\cdot 8\pi/5\cdot\eta^{-1/4} = 6.62\eta^{-1/4}. \tag{S54}$$

The equation above has exactly the same structure as Eq. (10) in the main text

$$\frac{\lambda}{L_r} = \alpha\eta^{-1/4}, \tag{S55}$$

where the prefactor α is found to lie within $6.71 < \alpha < 7.04$ depending on the values of λ/r_r. Finally, it is worth noting that if we take the limit for $\lambda/r_r \to +\infty$, Eq. (S53) and Eq. (9) in the main text yield exactly the same expression for the wavelength λ.

S7 Discrete elastic rod simulations

In Tab. S2 we summarize all parameters used in the 22 discrete elastic rod simulations we performed and the corresponding results. In all the simulations we considered a rod with length $L_r = 9.7$cm, diameter $d_r = 100\mu$m, density $\rho = 6500$kg/m^3, Young's modulus $E_r = 64.24$GPa and Poisson's ratio $\nu = 0.5$. We discretized the rod into 203 segments with $nv = 204$ nodes. The simulations were performed with control displacement boundary conditions, where one end of the rod was pined and the other end was displaced at a constant rate of $v_p = 0.05$mm/s.

[1] Note that the interaction energy constructed in this way does not account for the radius of the rod.

Table S2: BASim parameters and results. For each simulation, the dimensionless contact spring constant k_{dim}, the predicted buckling mode, the measured b/a for the minimum area ellipse, and also the buckled configurations are reported.

Simulation Parameters						
$\rho = 6500\mathrm{kg/m}^3$; $L_r = 9.7\mathrm{cm}$; $d_r = 100\mu\mathrm{m}$; $E_r = 64.24\mathrm{GPa}$; $G_r = 21.41\mathrm{GPa}$; $\nu = 0.5$; nv=204; $v_p = 0.05\mathrm{mm/s}$.						
ID	k_{dim}	mode number	b/a at $\epsilon = 5\%$	Cross-section view	Side view 1	Side view 2
1	400	4/5	0.13	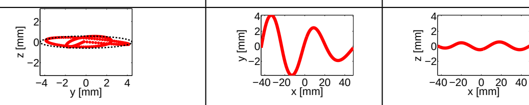		
2	525	5	0.00	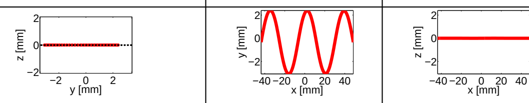		
3	650	5	0.00	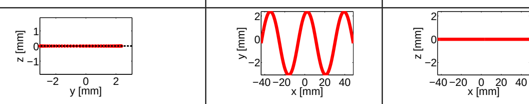		
4	775	5	0.00	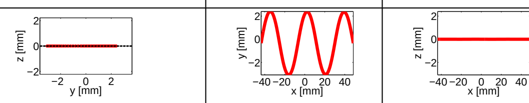		
5	900	5/6	0.30	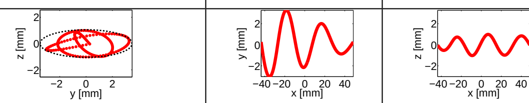		
6	1116	6	0.03	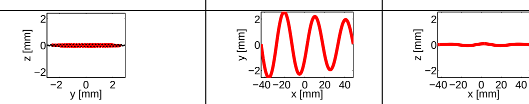		
7	1332	6	0.00	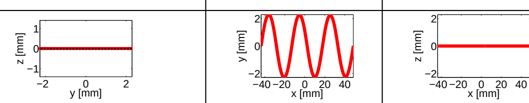		
8	1548	6	0.03	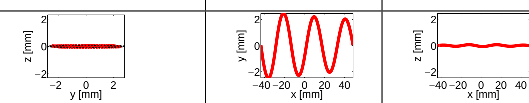		
9	1764	6/7	0.34	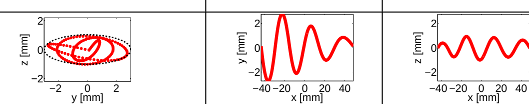		
10	2107	7	0.39	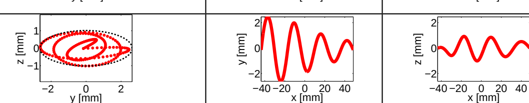		
11	2450	7	0.05	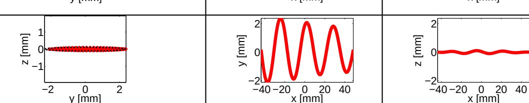		
12	2793	7	0.23	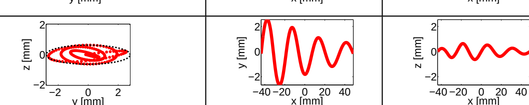		
13	3136	7/8	0.53	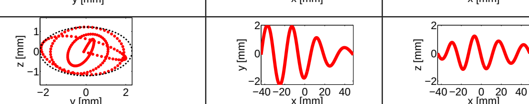		
14	3648	8	0.59	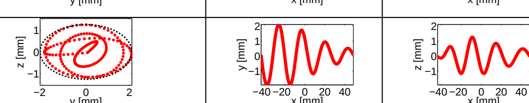		

Simulation Parameters						
$\rho = 6500\text{kg/m}^3$; $L_r = 9.7\text{cm}$; $d_r = 100\mu\text{m}$; $E_r = 64.24\text{GPa}$; $G_r = 21.41\text{GPa}$; $\nu = 0.5$; nv=204; $v_p = 0.05\text{mm/s}$.						
ID	k_{dim}	mode number	b/a at $\epsilon = 5\%$	Cross-section view	Side view 1	Side view 2
15	4160	8	0.40	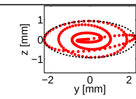	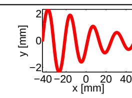	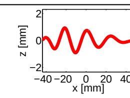
16	5184	8/9	0.82	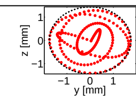	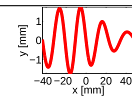	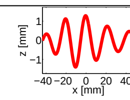
17	6642	9	0.86	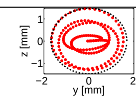	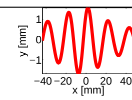	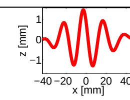
18	8100	9/10	0.94	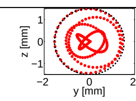	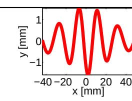	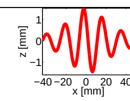
19	10100	10	0.97	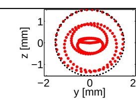	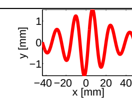	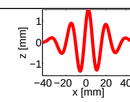
20	12100	10/11	1.00	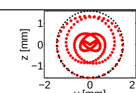	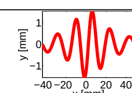	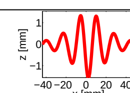
21	14762	11	0.97	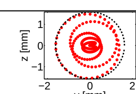	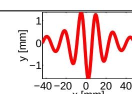	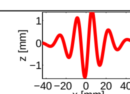
22	17424	11/12	0.96	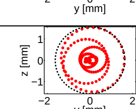	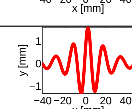	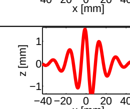

References

[1] A. N. Gent, *Engineering with Rubber: How to Design Rubber Components*, Hanser Publications, 2nd ed., 2001.

[2] F. Brau, H. Vandeparre, A. Sabbah, C. Poulard, A. Boudaoud and P. Damman, Multiple-length-scale elastic instability mimics parametric resonance of nonlinear oscillators, *Nat. Phys.*, 2011, **7**, 56-60.

[3] J. Nase, Debonding of viscoelastic materials: From a viscous liquid to a soft elastic solid, Ph.D. thesis, Universität des Saarlandes and Université Pierre et Marie Curie, 2009.

[4] X. Q. Brown, K. Ookawa, and J. Y. Wong, Evaluation of polydimethylsiloxane scaffolds with physiologically-relevant elastic moduli: interplay of substrate mechanics and surface chemistry effects on vascular smooth muscle cell response, *Biomaterials*, 2005, **26**, 3123-3129.

[5] D. S. Gray, J. Tien, and C. S. Chen, Repositioning of cells by mechanotaxis on surfaces with micropatterned young's modulus, *J. Biomed. Mater. Res. A.*, 2003, **66**, 605-614.

[6] I. T. Jolliffe, *Principal Component Analysis*, Springer, 2nd ed., 2002.

[7] M. Ringnér, What is principal component analysis? *Nat. Biotechnol.*, 2008, **26**, 303-304.

[8] L. R. Herrmann, W. E. Mason and S. T. K. Chan, Response of reinforcing wires to compressive states of stress, *J. Compos. Mater.*, 1967, **1**, 212-226.

[9] Y. Lanir and Y. C. B. Fung, Fiber composite columns under compression, *J. Compos. Mater.*, 1972, **6**, 387-401.

[10] C. P. Brangwynne, F. C. MacKintosh, S. Kumar, N. A. Geisse, J. Talbot, L. Mahadevan, K. K. Parker, D. E. Ingber and D. A. Weitz, Microtubules can bear enhanced compressive loads in living cells because of lateral reinforcement, *J. Cell Biol.*, 2006, **173**, 733-741.

[11] Wu J, Liu ZJ, Song J, Huang Y, Hwang KC, Zhang YW, Roger JA, Stretchability of encapsulated electronics, *Appl. Phys. Lett.*, 2011, **99**, 061911.

[12] Jiang H, Sun Y, Rogers JA, Huang Y, Post-buckling analysis for the precisely controlled buckling of thin film encapsulated by elastomeric substrates, *Int. J. Solids. Struct.*, 2008, **45**, 2014-2023.

[13] Jiang H, Zhang J, Mechanics of microtubule buckling supported by cytoplasm, *J. Appl. Mech.*, 2008, **75**, 061019.

[14] Huang ZY, Hong W, Suo Z, Nonlinear analyses of wrinkles in a film bonded to a compliant substrate, *J. Mech. Phys. Solids.*, 2008, **53**, 2101-2118.